Advanced Composites and Hybrid Materials (2023) 6:169
https://doi.org/10.1007/s42114-023-00731-3

RESEARCH

Graphene/polyacrylamide interpenetrating structure hydrogels for wastewater treatment

Xiufang Zhu[1,2] · Zelin Wang[1] · Jian Ren[1] · Najla AlMasoud[3] · Zeinhom M. El-Bahy[4] · Taghrid S.Alomar[3] · Chun Zhang[1] · Jun Zhang[1] · Juying Zhou[5] · Mufang Li[1,6] · Dong Wang[6] · Ilwoo Seok[8] · Xingkui Guo[7,9]

Received: 3 June 2023 / Revised: 16 August 2023 / Accepted: 22 August 2023 / Published online: 20 September 2023

Abstract

Developing efficient, cost-effective, and environmentally friendly wastewater treatment technologies is of great significance due to the increasingly serious global environmental issue. The direct discharge of wastewater containing a large amount of harmful substances from industrial activities and daily life has severe impacts on ecosystems and human health. Therefore, this study aims to address this issue by developing a novel graphene/polyacrylamide interpenetrating network hydrogel for wastewater adsorption. By interpenetrating graphene and polyacrylamide, the advantages of both materials can be fully utilized to enhance the efficiency and performance of hydrogel wastewater adsorption. In addition, tannic acid is innovatively used as a reducing agent, not only connecting the dispersed graphene layers but also acting as a reducing agent. The hydrogel was characterized by infrared spectroscopy, surface morphology, and adsorption performance in this study. It was found that the thermal decomposition temperature of the composite hydrogel was improved with increasing the graphene content. The equilibrium water absorption capacity of the composite hydrogel was approximately 300%, and the adsorption capacity for $NiCl_2$ was approximately 110.25 mg/g, demonstrating promising potential for practical applications. The reaction kinetics also conformed closely to the pseudo-second-order adsorption model, indicating an intraparticle diffusion model. This study provides an alternative hydrogel for treating wastewater.

Keywords Wastewater · Graphene · Hydrogel · Tannic acid · Acrylamide · Adsorption capacity

1 Introduction

Wastewater that is discharged directly into the aquatic environment without proper treatment not only causes significant pollution but also poses a considerable risk to human health [1–3]. Over the past few decades, numerous technologies have been employed for wastewater treatment, including adsorption [4–7], oxidation [8], electrocoagulation [8], chemical precipitation [9], flocculation [10], membrane filtration [11–14], electrolysis [15, 16],

✉ Jun Zhang
magicaincn@126.com

✉ Juying Zhou
zhoujuying@126.com

✉ Ilwoo Seok
iseok@astate.edu

✉ Xingkui Guo
guoxingkui@u.nus.edu

1 School of Materials Science and Engineering, Hubei University of Automotive Technology, Shiyan 442002, China

2 Longzhong Laboratory, Xiangyang 441000, China

3 Department of Chemistry, College of Science, Princess Nourah bint Abdulrahman University, P.O. Box 84428, Riyadh 11671, Saudi Arabia

4 Department of Chemistry, Faculty of Science, Al-Azhar University, Nasr City, Cairo 11884, Egypt

5 Key Laboratory of Chemistry and Engineering of Forest Product, Guangxi Key Laboratory of Chemistry and Engineering of Forest Products, Guangxi University for Nationalities, Nanning 530006, China

6 Key Laboratory of Textile Fibers and Products, Ministry of Education, Wuhan Textile University, Wuhan 430200, China

7 Department of Materials Science and Engineering, National University of Singapore, Singapore 117574, Singapore

8 College of Engineering and Computer Science, Arkansas State University, Jonesboro, AR 72467, USA

9 College of Materials Science and Engineering, Taiyuan University of Science and Technology, Taiyuan 030024, China

catalytic degradation [17, 18], and biological degradation [19]. However, these technologies have their own limitations, such as prolonged processing time, high expenses, complex operation, and susceptibility to environmental factors, which impede their practical implementation in wastewater treatment. Among these techniques, adsorption stands out as a highly promising method for removing heavy metal ions due to its advantages of affordability, effectiveness, and environmental safety [20–23].

Hydrogels with high water absorption and adsorption capacities have gained significant attention [24–32]. Notably, the double-mesh interpenetrating hydrogel technology and nanocomposite hydrogel technology have made remarkable advancements in this field [33, 34]. Graphene oxide (GO) is widely used in various applications, including wastewater treatment [35], electrical conductivity [36], composites [37], energy conversion/storage units [38], and sensing [39], due to its excellent hydrophilicity and adsorption properties resulting from its large specific surface area. Similarly, MXene and carbon nanotubes demonstrate advantageous characteristics such as high specific surface area, excellent mechanical properties, and conductivity. However, they have relatively fewer surface functional groups, leading to weaker interactions with polyacrylamide and potentially limited enhancement of hydrogel performance. In the synthesis of graphene hydrogel, Ma et al. employed a unique approach by incorporating water within its structure, resulting in distinct adsorption properties for complex systems containing Cu(II) and ciprofloxacin (CIP) compared to normal minerals [40]. Batch adsorption experiments yielded the following conclusions: adsorbed Cu(II) acts as a bridge, while dissolved Cu(II) acts as a competitor. The GH-CIP-Cu(II) ternary complex model successfully explains the increased Cu(II) adsorption. Water present at the interface can provide adsorption sites through hydrogen bonds or act as a barrier for Cu(II) and CIP adsorption. Considering the environmental behavior of complex pollutants, it is essential to consider the role of bound water to comprehensively understand the process and mechanism. Furthermore, the positive influence of enclosed water can be integrated into the design of hydrogel adsorbents.

In wastewater treatment, when hydrogels are directly placed in heavy metal ion effluent, their powder-like properties can result in secondary pollution due to the difficulties in recovery after adsorption. The physical co-blending of graphene with the above two materials cannot effectively immobilize it in the hydrogel. Therefore, it is critical to investigate new water-absorbent gel materials with superior adsorption properties and high mechanical strength. This study focuses on utilizing a reduction method to cross-link the chemical groups on the surface of graphene, forming an interpenetrating network structure hydrogel, and leveraging the synergistic effect of both components for wastewater adsorption. Existing literature commonly employs the reducing agent hydrazine hydrate, which is environmentally polluting, and hydrothermal synthesis, characterized by high temperatures, long reaction times, and high energy consumption. Tannic acid, a natural reducing agent, efficiently reduces metal ions [41, 42], thereby facilitating fast reactions at low temperatures. Additionally, tannic acid exhibits diverse biological activities such as antioxidant, antibacterial, and anti-inflammatory effects, making it widely applicable in medicine, food, and cosmetics.

In this study, the formation of interpenetrating network structure (IPN) to obtain graphene/polyacrylamide interpenetrating network hydrogels was controlled by temperature. Tannic acid, a plant extract, was used both as a reducing agent and to connect the dispersed graphene lamellae. This choice aligns with the environmental green concept. Subsequently, the surface morphology, thermal stability, swelling, and adsorption behavior of the hydrogels were investigated.

2 Experimental section

2.1 Chemicals and instruments

The instrument and materials used include ZL-12TD-type freeze dryer (Shanghai Zuole); IRAFFINITY-1-type Fourier infrared spectrum analyzer; UV-2045-type ultraviolet visible photometer (Shimadzu, Japan); JSM-7900F-type field emission scanning electron microscope (Japan Electronics Co., Ltd.); SBC-12-type ion sputtering instrument (Beijing Zhongke Keji); and Q600SDT-type synchronous thermal analyzer (TA, USA).

N,N-methylenebisacrylamide (MBA, BASF Tianjin Chemical Co., Ltd.); acrylamide (AM), Comio reagent; tannic acid (TA, tannic acid, West Asia Reagent Co., Ltd.); and graphene oxide (GO, Shenzhen Hongda Chang Co., Ltd.) were used as received without any further treatment.

2.2 Preparation of IPN hydrogels

To obtain a homogeneous graphene oxide solution, graphene oxide powder was added to deionized water and thoroughly shaken for 6 h using ultrasonic waves. Acrylamide, tannic acid, cross-linking agent N,N-methylenebisacrylamide (MBA), and deionized water were then taken and mixed well. The mixture was heated in a water bath to 90 °C until all substances were fully dissolved. Afterward, initiator ammonium persulfate (APS) was added to the solution, which was rapidly shaken. The resulting mixture was poured into a 50-mL beaker and maintained at a temperature of 60 ℃. The reaction was allowed to proceed for 3 h, resulting in the formation of polyacrylamide hydrogel. Next, the oven

temperature was increased to 90 ℃ and maintained for 8 h to obtain the desired product. The prepared gel was then placed in a dialysis bag and soaked with deionized water for 72 h, with the water being replaced every 6 h to remove any unreacted tannins from the gel. Finally, the sample was freeze dried and prepared, and the detailed formulations can be found in Table 1.

2.3 FTIR characterization

The samples to be characterized were prepared using the KBr press method. First, KBr was dried in an oven. Then, small amounts of lyophilized hydrogel sample, tannic acid, and graphene oxide were powdered together with KBr in an agate mortar. The mixture was then made into a transparent sheet using a press. Next, the samples were tested in an infrared spectrometer to obtain the characteristic absorption peaks of the corresponding functional groups. The scanning range was in the mid-infrared region and the scanning frequency was 1 time/s. Infrared spectroscopy is a commonly used analytical tool to identify macromolecular compounds and determine their molecular structure.

2.4 Scanning electron microscopy observation

The freeze-dried hydrogel samples were cut into strips measuring 4 mm in length and 2 mm in height and width. These strips were then glued to the SEM sample stage using conductive tape and sprayed with gold on the surface to observe the hydrogel's surface morphology using SEM.

2.5 Water absorption test

The freeze-dried samples of PAM (100%), GO-PAM (1%), and GO-PAM (2%) were weighed and placed in a 25-mL centrifuge tube. Then, 15 mL of deionized water was added to fully swell the samples for 24 h. This process is used to determine the water absorption rate, as indicated by Eq. (1).

$$Q(\%) = \left(\frac{m_0 - m_0}{m_0}\right) \times 100\% \quad (1)$$

where Q is the water absorption rate; m_0 is the mass of the sample after lyophilization; m_t is the sample mass after water absorption equilibrium of the specimen.

Table 1 Hydrogel preparation formulations

Samples	AM/g	TA/mg	GO/mg
100% PAM	1.8	0	0
2%GO-PAM	1.8	5	4
1%GO-PAM	1.8	5	2

2.6 Thermal gravimetric analysis

A dried hydrogel sample weighing approximately 10 mg underwent measurement using a Q600SDT-type simultaneous thermal analyzer. The analysis was conducted under a nitrogen atmosphere, with a nitrogen flow rate of 10 mL/min and a heating rate of 10 °C/min. The temperature range was set from 25 to 600 °C.

2.7 Heavy metal ion adsorption test

The prepared standard samples were plotted on a UV spectrophotometer after configuring 5 gradients of nickel chloride solution to prepare the nickel chloride solution. Then, 50 mg of lyophilized graphene hydrogels was added to centrifuge tubes containing 20 mL of nickel chloride solution in 5 concentration gradients. After shaking for 1 h, the upper clear layer of the adsorbed solution was taken. The absorbance and concentration changes of the adsorbed solution were measured using a UV spectrophotometer. Finally, the removal rate of heavy metal ions was obtained by comparing the before and after concentration changes.

The adsorption capacity of graphene hydrogels was investigated by comparing it under different conditions. In this study, 15 mg of graphene hydrogel samples was added to a beaker containing 100 mL of a nickel chloride solution with a concentration of 30 mg/L. The experiment was conducted at 25 °C with a neutral pH value, and the mixture was shaken to promote adsorption. At specific time intervals (i.e., 10, 20, 30, 40, 50, 60, and 80 min), the remaining nickel chloride content of the adsorbed solution was measured using a UV spectrophotometer. By obtaining the adsorption capacity of the hydrogel at adsorption equilibrium, the kinetics of adsorption were further investigated.

3 Results and discussion

3.1 Analysis of FTIR measurements results

The FTIR spectra of graphene oxide, hydrogel, and tannic acid were obtained through FTIR characterization (Fig. 1a) as shown below, from top to bottom. The presence of oxygen-containing groups, such as carboxyl, hydroxyl, carbonyl, and ether bonds, leads to the oxidation of graphene, which is evident from the FTIR spectrum. The characteristic peaks of these groups can be observed. The stretching vibration of the –OH functional group is located at around 3404 cm^{-1} in the high-frequency region [43, 44]. The broad peak spectrum in this range is attributed to the existence of water molecules in GO. Additionally, the absorption peaks observed in the mid-frequency region at approximately 1719 cm^{-1} correspond to the carboxyl and

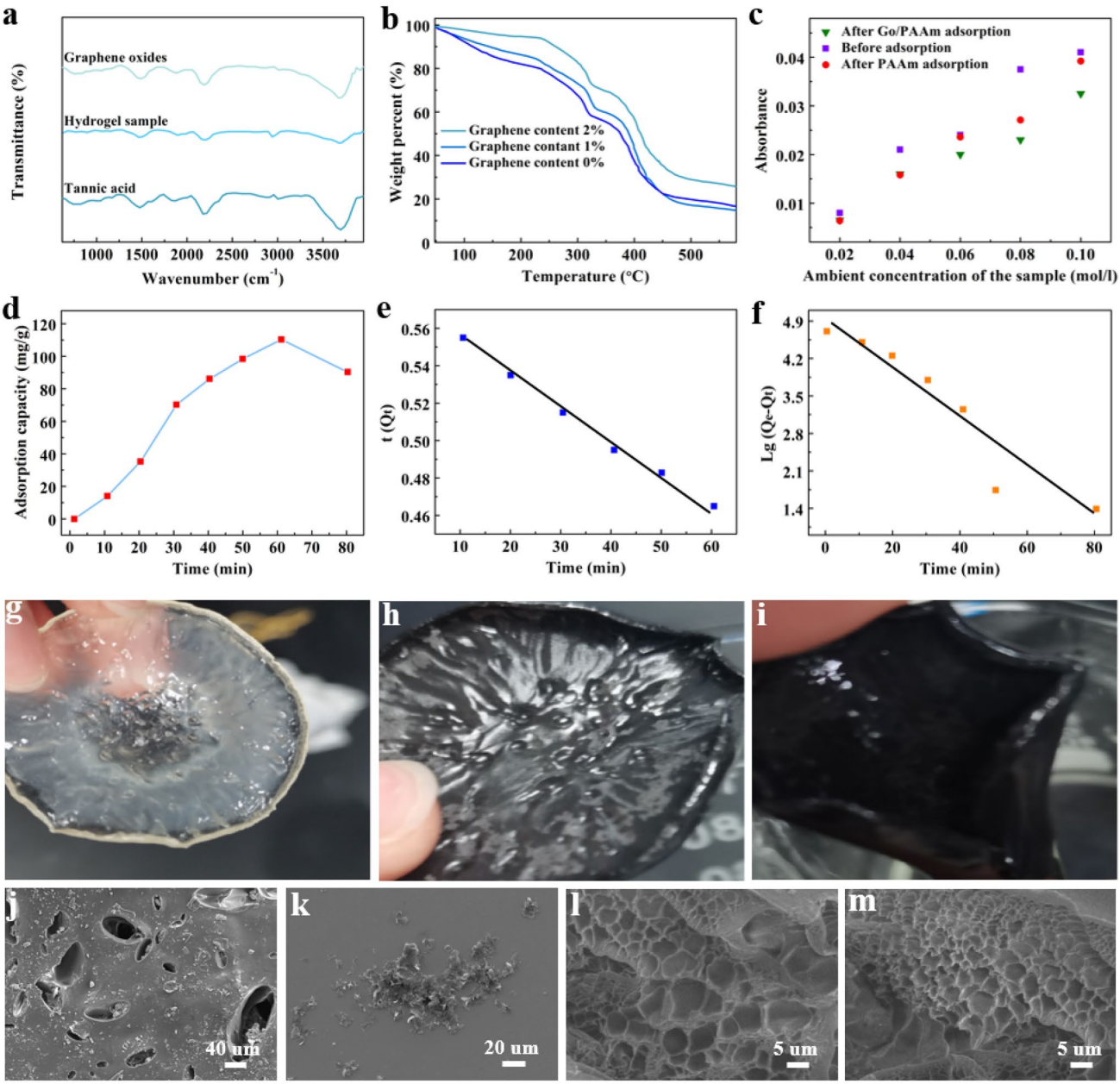

Fig. 1 Graph generated from experimental data of graphene hydrogel processed using Origin: **a** Infrared spectrum of GO (2% GO-PAM), TA; **b** thermogravimetric curves of the hydrogel series samples; **c** comparison of absorbance of solution before and after adsorption by PAAm and Go/PAAm hydrogels; **d** graphite alkene hydrogel adsorption capacity versus time curve; **e** hydrogel adsorption $Ni2^{+}$ quasi primary kinetic fitting curve; **f** quasi-secondary kinetic fitting curve for $Ni2^{+}$ adsorption by hydrogel. Hydrogel sample diagram: **g** 0%GO-PAM; **h** 1%GO-PAM; **i** 2%GO-PAM. SEM photograph: **j** SEM image of graphene oxide hydrogel; **k** SEM image of graphene flakes; **l** SEM image of cross-section of 1% GO-PAM hydrogel; **m** SEM image of cross-section of 2% GO-PAM hydrogel

carbonyl C=O stretching vibrations at the edge of the GO lamellae [45, 46]. Furthermore, the stretching vibrations of the C–O–C ether bond result in the formation of the peak at 1054 cm^{-1}, while the peak at 875 cm^{-1} is associated with the stretching vibration of the epoxy group.

The FTIR spectra of GO and 2% GO-PAM were compared. The reduced graphene oxide hydrogels showed generally weaker characteristic absorption peaks of oxygen-containing groups. This phenomenon was attributed to the reduction of graphene oxide by tannic acid, leading to the removal of most oxygen-containing functional groups in the lamellae [1]. In addition, the reduced graphene oxide hydrogels had less pronounced characteristic peaks in the FTIR spectra.

The graphene/polyacrylamide interpenetrating network hydrogel exhibits several characteristic peaks. One such peak

is the vibrational absorption peak of the amine group ($–NH_2$) in polyacrylamide, which can be observed at 3438 cm^{-1}. Another noteworthy absorption peak is found between the range of 1725 to 1740 cm^{-1}. This peak is associated with the reaction between the phenolic hydroxyl group in TA and the carboxyl group of graphene oxide, resulting in the formation of an ester group. Simultaneously, there are strong absorption peaks at 1694 cm^{-1} and 1638 cm^{-1}. These peaks are attributed to the stretching vibration of the carbon-oxygen double bond in the amide group (–C=O) and the bending vibration of the amine group ($–NH_2$).

The phenolic hydroxyl characteristic absorption peak in tannic acid, observed in its FTIR spectrum, is found at 3354 cm^{-1}. After hydrolysis to gallic acid, this peak remains present. In reduced graphene oxide hydrogel, however, the –OH peak is relatively weaker compared to that of tannic acid. This suggests that tannic acid interacts with graphene oxide, leading to a consumption of –OH groups.

3.2 Scanning electron microscopy analysis

The surface morphology of the experimentally prepared hydrogel samples was analyzed using scanning electron microscopy. The figure below illustrates the results of the analysis (see Fig. 1j). It is evident from the figure that the graphene hydrogel exhibits a distinct pore structure, with clearly visible layers of graphene flakes on the surface. On the other hand, Fig. 1k depicts the structure of graphene oxide. It can be observed that the graphene oxide utilized in the experiment is a monolayer graphene oxide, with a sheet diameter ranging from approximately 7 to 15 μm.

The observed cross-section of 1% GO-PAM hydrogel and 2% GO-PAM hydrogel showed that the pore size of the hydrogel with 2% graphene content is approximately 5 μm, while the pore size of the hydrogel with 1% graphene content is about 10 μm (Fig. 1l, m). After freeze drying under the same conditions as the hydrogel with 1% graphene content, it was observed that the pore size of the hydrogel with 2% graphene content is relatively smaller and denser [47]. This suggests that an appropriate increase in the amount of GO leads to a further reduction in pore size. This reduction is attributed to the redox reaction between tannic acid and reduced graphene oxide in the hydrogel skeleton, resulting in the formation of ester groups which connect the graphene lamellae together. Furthermore, the reduced graphene oxide interacts through π-π bonds and forms a three-dimensional network structure, thereby further reducing the pore size.

Tannic acid reacts with graphene oxide in a graphene hydrogel, resulting in the formation of reduced graphene oxide. This reaction chemically bonds the two substances and immobilizes the graphene securely inside the hydrogel through the IPN structure.

3.3 Thermodynamic analysis

Figure 1b shows the thermal weight loss curves of graphene hydrogels with varying graphene oxide (GO) contents, as tested by a thermodynamic analyzer. The addition of graphene oxide has a noticeable impact on the thermal degradation trend of the acrylamide hydrogel. Specifically, when different levels of graphene are incorporated into the hydrogel, the thermal weight loss temperature of the hydrogel increases. This effect can be attributed to the presence of the graphene oxide sheet layer within the hydrogel. The physical barrier created by this layer affects the internal heat transfer and provides protection for a portion of the hydrogel's internal structure.

The addition of GO to the hydrogel led to an increase in the thermal weight loss temperature, as shown in Table 2. Specifically, the thermal weight loss temperature of 1% GO-PAM increased by 24 °C, and for 2% GO-PAM, it increased by 30 °C. Similarly, the hydrogel T10% exhibited an increase in the thermal weight loss temperature; with the thermal weight loss temperature of 1% GO-PAM and 2% GO-PAM increasing by 16 °C and 18 °C, respectively. This response was even more pronounced for the hydrogel T50%, as the thermal weight loss temperature of 1% GO-PAM and 2% GO-PAM increased by 18 °C and 16 °C, respectively. The enhanced thermal properties of the composite hydrogel can be attributed to the physical barrier created by the larger specific surface area of GO, impeding the polymer chains, as well as the unique thermal conductivity of GO hindering the decomposition of the polymer chains. These findings suggest that the reaction of GO sheets with tannic acid played a cross-linking role in the graphene/polyacrylamide interpenetrating network hydrogel structure [48].

3.4 Analysis of water absorption results

The data in Table 3 demonstrates the water absorption capabilities of the acrylamide hydrogel, which improve with the addition of graphene oxide. It can be observed that polyacrylamide exhibits good water absorption. Furthermore, the addition of graphene oxide leads to an increase in water absorption by 8% and 30%, respectively. This enhanced water absorption can be attributed to the

Table 2 The temperature corresponding to the degree of weight loss of hydrogel series samples

Samples	*T* initial/mg	$T_{10\%}$ /mg	$T_{10\%}$ /℃	$T_{50\%}$ /mg	$T_{50\%}$ /℃
100% PAM	10.29	9.26	131.4	5.14	392.8
1%GO-PAM	9.83	8.84	155.6	4.91	408.5
2%GO-PAM	11.27	10.14	185.7	5.63	426.4

Table 3 Measurement data of water absorption of hydrogel series samples

Samples	Mass before water absorption/g	Mass after water absorption/g	Water absorption %
100% PAM	0.2747	1.0528	283
1%GO-PAM	0.1807	0.7066	291
2%GO-PAM	0.2473	1.0658	313

presence of oxygen-containing hydrophilic functional groups on the surface of graphene and the formation of interconnected pores when the graphene sheets are joined, resulting in improved water absorption.

3.5 Adsorption behavior analysis

3.5.1 Removal rate of heavy metal ions in specific solutions

The adsorption efficiency of graphene hydrogel varies with the concentration, as evidenced by the data presented in Fig. 1c and Tables 4 and 5. Specifically, the adsorption effect improves as the concentration of the solution increases. The unique three-dimensional network structure of the hydrogel, combined with the reaction between graphene and tannic acid, results in the formation of denser and narrower pores inside the hydrogel. This characteristic prevents the diffusion of heavy metal ions from the adsorption equilibrium. Notably, the adsorption equilibrium can be reached in approximately 60 min [49]. Furthermore, the adsorption efficiency is directly influenced by the concentration of the solution being adsorbed. The changes in absorbance before and after adsorption are represented by Eq. (2):

$$Q(\%) = \frac{c_{0-}c_t}{c_0} * 100\% \tag{2}$$

where Q is the adsorption rate; C_0 is the concentration of nickel chloride before adsorption in Eq. (2); C_t is the concentration of nickel chloride after adsorption.

Table 4 Removal rate data of heavy metal ions by PAAm hydrogel adsorption

Sample Serial number	Pre-sorption concentration mol/L	Concentration after adsorption mol/L	Removal rate %
1	0.02	0.012	38.6
2	0.04	0.031	21.1
3	0.06	0.047	20.5
4	0.08	0.056	29.2
5	0.10	0.080	20

Table 5 Removal rate data of heavy metal ions by GO/PAAm hydrogel adsorption

Sample Serial number	Pre-sorption concentration mol/L	Concentration after adsorption mol/L	Removal rate %
1	0.02	0.015	25
2	0.04	0.029	27.5
3	0.06	0.044	26.7
4	0.08	0.055	31.25
5	0.10	0.072	28

The sample used in the experiment is 50 mg of 2% GO-PAM dry glue

3.5.2 Adsorption capacity of graphene hydrogels

The concentration of heavy metal ions in solution is measured by UV-Vis spectrophotometer and the adsorption capacity can be calculated by Eq. (3):

$$q_e = \frac{c_0 - c_e}{m} v \tag{3}$$

where C_0 (mg/L) and C_e (mg/L) denote the initial concentration of the solution and the concentration when the adsorption equilibrium is reached, respectively; m (g) denotes the input mass of the graphene hydrogel; V (L) refers to the volume of the solution used for the adsorption experiment.

Figure 1d shows the curve of adsorption capacity measurement. The adsorption capacity of graphene hydrogel can reach 108.34 mg/g, which is comparable to the adsorption capacity reported in the literature. (The maximum adsorption capacity of layer-by-layer structured chitosan/graphene oxide composite hydrogel for Ni^{2+} is 121.58 mg/g, as measured by Li et al. [50].)

3.5.3 Adsorption kinetics

The first-stage adsorption uses the Largergen equation to calculate the adsorption rate, which is shown by Eq. (4):

$$\frac{d_{Q_t}}{d_t} = k_1(Q_e - Q_t) \tag{4}$$

where Q_e represents the adsorption capacity of the adsorbent used for adsorption when it reaches adsorption equilibrium; Q_t represents the adsorption capacity (mg/g) of the hydrogel at any adsorption moment t; and k_1 is a constant which represents the quasi-level adsorption rate constant in (min^{-1}).

By conducting data processing on both sides of (4) and integrating from $t = 0$ to $t > 0$, Eq. (5) is obtained.

$$\ln\left(Q_e - Q_t\right) = -K_1 t + \ln Q_e \tag{5}$$

for $\ln(Q_e - Q_t)$ vs. t, plotting $\ln(Q_e - Q_t)$ as the vertical axis and t time as the horizontal axis after data processing in

Table 6 Adsorption capacity of graphene hydrogels with time at the same concentration gradient

Sample adsorption time/min	Concentration of the upper layer of clear liquid at the time of sampling mg/L	Adsorption capacity mg/g
0	30	0
10	27.3	18
20	24.4	37.34
30	21.3	58
40	17.9	80.67
50	15.1	99.34
60	14.2	108.34
80	14.8	101.33

The sample used in the experiment is 15 mg of 2% GO-PAM dry glue

origin to do data analysis, the quasi-level kinetic fitting curve was obtained. As in Fig. 1e, the secondary model of adsorption kinetics is based on chemisorption. The specific expression of the quasi-secondary kinetic equation is shown in Eq. (6):

$$\frac{d_{Q_t}}{d_t} = k_2(Q_e - Q_t)^2 \tag{6}$$

In the formula, Q_e and Q_t have the same meaning as in formula (6); k_2 indicates the secondary adsorption rate constant (g/mg-min).

Similarly integrating the above equation, Eq. (7) was formed:

$$\frac{t}{Q_t} = \frac{1}{K_2 Q_e^2} + \frac{t}{Q_e} \tag{7}$$

Plotting t/Q_t against t, a first-order kinetic fitting curve was obtained, as shown in Fig. 1f.

The adsorption of heavy metal ions onto nickel chloride solutions was conducted using graphene/acrylamide interpenetrating network hydrogels. The data in Table 6 were obtained by fitting the theoretical adsorption capacity and kinetic related parameters.

Based on the analytical results presented in Table 7 and Fig. 1e, f, the fitted quasi-level dynamic equations

Table 7 Parameters related to quasi-primary and quasi-secondary kinetics of nickel chloride adsorption by adsorbent graphene hydrogels

Quadratic kinetic equations			Quasi-secondary kinetic equation		
$\ln(Q_e - Q_t) = -K_1 t + \ln Q_e$			$\frac{t}{Q_t} = \frac{1}{K_2 Q_e^2} + \frac{t}{Q_e}$		
Qe	k_1	R^2	Qe	k_2	R^2
103.35 mg/g	0.180	0.89114	110.25 mg/g	0.0021	0.99708

The hydrogel sample used for the adsorption capacity determination was 2% GO-PAM dry gel with a mass of 15 mg

R^2 and quasi-secondary dynamic equations R^2 in Origin were found to be 0.89144 and 0.99708, respectively. Furthermore, the equilibrium adsorption capacity Q_e value of 110.25 mg/g obtained from the analysis was found to be more similar to the experimental result of 108.34 mg/g. These results indicate that the kinetic behavior of nickel chloride adsorption by graphene hydrogel was more consistent with the quasi-secondary kinetic model, as opposed to the quasi-level dynamic model.

4 Conclusions

By preparing the interpenetrating network structure hydrogel, it has been observed that the thermal stability of 2% GO-PAM is better than 1% GO-PAM. At T10% (10% thermal weight loss) of the hydrogel, the temperatures of 1% GO-PAM and 2% GO-PAM increased by 24 °C and 30 °C, respectively. Similarly, at T50% of the hydrogel, the thermal weight loss temperature of 1% GO-PAM and 2% GO-PAM increased by 16 °C and 18 °C, respectively. Moreover, the addition of graphene resulted in an increase in the equilibrium swelling rate of the hydrogel. The water absorption rate was 283% for 100% PAM, 291% for 1% GO-PAM, and 313% for 2% GO-PAM. This indicates that 1% GO-PAM increased by 8% compared to 100% PAM, while 2% GO-PAM increased by 22% compared to 1% GO-PAM. Furthermore, the interpenetrating network graphene hydrogel prepared during dynamic adsorption showed good adsorption capacity of 108.34 mg/g. The process of adsorption of Ni^{2+} followed the quasi-secondary kinetic model. In summary, the preparation of the interpenetrating network structure hydrogel results in improved thermal stability, water absorption, and adsorption capacity. These findings suggest promising application prospects.

Author contribution Xingkui Guo and Jun Zhang conceived and supervised the research. Xiufang Zhu, ZelinWang, and Jian Ren carried out the materials preparation. Xiufang Zhu, Chun Zhang, Mufang Li, and Dong Wang performed sample characterization and test. Xiufang Zhu, Jun Zhang, Juying Zhou, Najla AlMasoud, Zeinhom M. El-Bahy, Taghrid S. Alomar, Ilwoo Seok, and Xingkui Guo analyzed data and wrote the manuscript. All authors participated in discussion, revision, and approval of the manuscript.

Funding We acknowledge the financial support from the Regional Innovation and Development Joint Fund of the National Natural Science Foundation of China (U20A20257) and the National Natural Science Foundation of China (52063004). The authors acknowledge the financial support from Princess Nourah bint Abdularahman University Researchers Supporting Project number (PNURSP2023R18), Princess Nourah bint Abdularahman University, Riyadh, Saudi Arabia.

Data availability The datasets generated during and/or analyzed during the current study are available from the corresponding author on reasonable request.

Declarations

Conflict of interest The authors declare no competing interests.

References

1. Wang Y, Lu H, Wang Y, Qiu J, Wen J, Zhou K, Chen L, Song G, Yao J (2016) Facile synthesis of TaO_xN_y photocatalysts with enhanced visible photocatalytic activity. RSC Adv 6:1860–1864. https://doi.org/10.1039/C5RA23087J
2. Wang C, Liu X, Yang T, Sridhar D, Algadi H, Xu BB, El-Bahy ZM, Li H, Ma Y, Li T, Guo Z (2023) An overview of metal-organic frameworks and their magnetic composites for the removal of pollutants, Sep Purif Technol 320:124144. https://doi.org/10.1016/j.seppur.2023.124144
3. Yang S, Shi C, Qu K, Sun Z, Li H, Xu B, Huang Z, Guo Z (2023) Electrostatic self-assembly cellulose nanofibers/MXene/nickel chains for highly stable and efficient seawater evaporation and purification. Carbon Lett 1–12. https://doi.org/10.1007/s42823-023-00540-0
4. Wen Y, Xue Y, Cui Z, Wang Y (2015) Thermodynamics of nanoadsorption from solution: Theoretical and experimental research. J Chem Thermodyn 80:112–118. https://doi.org/10.1016/j.jct.2014.08.013
5. Ji S, Song S, Zhao X (2021) Selective adsorption and separation of dyes from aqueous solution by a zirconium-based porous framework material. Appl Organomet Chem 35:e6314. https://doi.org/10.1002/aoc.6314
6. Zhao X (2021) The application of MOFs-based materials for antibacterials adsorption. Coord Chem Rev 440:213970. https://doi.org/10.1016/j.ccr.2021.213970
7. Zhang J, Yang J, Cheng L, Wang Y, Feng G (2018) Adsorption of acetylene on Sn-doped Ni(111) surfaces: a density functional study. J Mol Model 26:310. https://doi.org/10.1007/s00894-020-04568-1
8. Si Y, Li J, Cui B, Tang D, Yang L, Murugadoss V, Maganti S, Huang M, Guo Z (2022) Janus phenol-formaldehyde resin and periodic mesoporous organic silica nanoadsorbent for the removal of heavy metal ions and organic dyes from polluted water. Adv Compos Hybrid Mater 5:1180–1195. https://doi.org/10.1007/s42114-022-00446-x
9. Das PP, Sharma M, Purkait MK (2022) Recent progress on electrocoagulation process for wastewater treatment: A review Sep Purif Technol 292:121058. https://doi.org/10.1016/j.seppur.2022.121058
10. Kang J, Sun W, Hu Y, Gao Z, Liu R, Zhang Q, Liu H, Meng X (2017) The utilization of waste by-products for removing silicate from mineral processing wastewater via chemical precipitation. Water Res 125:318–324. https://doi.org/10.1016/j.watres.2017.08.047
11. Lin C, Liu B, Pu L, Sun Y, Xue Y, Chang M, Li X, Lu X, Chen R, Zhang J (2021) Photocatalytic oxidation removal of fluoride ion in wastewater by g-C3N4/TiO_2 under simulated visible light. Adv Compo Hybrid Mater 4:339–349. https://doi.org/10.1007/s42114-021-00228-x
12. Liu M, Li P, Meng Q, Ge Q (2021) Membranes constructed by metal-ligand complexation for efficient phosphorus removal and fouling resistance in forward osmosis. Adv Compos Hybrid Mater 5:159–172. https://doi.org/10.1007/s42114-021-00254-9
13. Huang JH, Cheng XQ, Wu YD, Zhang YQ, Li SW, Lau CH, Shao L (2021) Critical operation factors and proposed testing protocol of nanofiltration membranes for developing advanced membrane materials. Adv Compos Hybrid Mater 4:1092–1101. https://doi.org/10.1007/s42114-021-00334-w
14. Ding Z, Tian Z, Ji X, Dai H, Si C (2022) Bio-inspired catalytic one-step prepared R-siloxane cellulose composite membranes with highly efficient oil separation. Adv Compos Hybrid Mater 5:2138–2153. https://doi.org/10.1007/s42114-022-00517-z
15. Cheng XQ, Li S, Bao H, Yang X, Li Z, Zhang Y, Wang K, Ma J, Ullah A, Shao L (2021) Poly(sodium-p-styrenesulfonate)-grafted UiO-66 composite membranes boosting highly efficient molecular separation for environmental remediation. Adv Compos Hybrid Mater 4:562–573. https://doi.org/10.1007/s42114-021-00253-w
16. Yao F, Zhang W, Hu D, Li S, Kong X, Uemura S, Kusunose T, Feng Q (2022) Ultra-hydrophilic nanofiltration membranes fabricated via punching in the HTO nanosheets. Adv Compo Hybrid Mater 6:1–16. https://doi.org/10.1007/s42114-022-00579-z
17. Huang J, Lu X, Zhang X (2022) Transient computational fluid dynamics simulation of pulse feed in vacuum membrane distillation process. Adv Compos Hybrid Mater 5:2515–2526. https://doi.org/10.1007/s42114-022-00502-6
18. Sun P, Zhou S, Yang Y, Liu S, Cao Q, Wang Y, Wågberg T, Hu G (2022) Artificial chloroplast-like phosphotungstic acid-iron oxide microbox heterojunctions penetrated by carbon nanotubes for solar photocatalytic degradation of tetracycline antibiotics in wastewater. Adv Compos Hybrid Mater 5:3158–3175. https://doi.org/10.1007/s42114-022-00462-x
19. Li Z, Xie W, Yao F, Du A, Wang Q, Guo Z, Gu H (2022) Comprehensive electrocatalytic degradation of tetracycline in wastewater by electrospun perovskite manganite nanoparticles supported on carbon nanofibers. Adv Compos Hybrid Mater 5:2092–2105. https://doi.org/10.1007/s42114-022-00550-y
20. Dai L, Li X, Zhang L, Ma P, Guan J, Yu W (2022) Facile preparation of FL-Ti_3C_2/BiOCl/SnO_2 ternary composite for photocatalytic degradation of indoor formaldehyde. Adv Compos Hybrid Mater 5:2285–2296. https://doi.org/10.1007/s42114-021-00398-8
21. Guo X, Yang F, Sun X, Han C, Bai Y, Liu G, Liu W, Wang R (2022) Fabrication of a novel separation-free heterostructured photocatalyst with enhanced visible light activity in photocatalytic degradation of antibiotics. J Mater Chem A 10:3146–3158. https://doi.org/10.1039/d1ta09757a
22. Zeng J, Xie W, Guo Y, Zhao T, Zhou H et al (2024) Magnetic field facilitated electrocatalytic degradation of tetracycline in wastewater by magnetic porous carbonized phthalonitrile resin. Appl Cat B: Environ 340:123225. https://doi.org/10.1016/j.apcatb.2023.123225
23. Kegl T, Košak A, Lobnik A, Novak Z, Kralj AK, Ban I (2020) Adsorption of rare earth metals from wastewater by nanomaterials: A review. J Hazard Mater 386: 121632. https://doi.org/10.1016/j.jhazmat.2019.121632
24. Ma Y, Lv L, Guo Y, Fu Y, Shao Q, Wu T, Guo S, Sun K, Guo X, Wujcik EK, Guo Z (2017) Porous lignin based poly (acrylic acid)/organo-montmorillonite nanocomposites: Swelling behaviors and rapid removal of Pb (II) ions. Polymer 128:12–23. https://doi.org/10.1016/j.polymer.2017.09.009
25. Guo X, Yang F, Sun X, Bai Y, Liu G, Liu W, Wang R, He X (2022) Anti-freezing self-adhesive self-healing degradable touch panel with ultra-stretchable performance based on transparent triboelectric nanogenerators. Adv Func Mater 32:2201230. https://doi.org/10.1002/adfm.202201230
26. Guo X, Yang F, Liu W, Han C, Bai Y, Sun X, Hao L, Jiao W, Wang R (2021) Skin-inspired self-healing semiconductive touch panel based on novel transparent stretchable hydrogels. J Mater Chem A 9:14806–14817. https://doi.org/10.1039/d1ta01892b
27. Liu J, Chen E, Wu Y, Yang H, Huang K, Chang G, Pan X, Huang K, He Z, Lei M (2022) Silver nanosheets doped polyvinyl alcohol hydrogel piezoresistive bifunctional sensor with a wide range and high resolution for human motion detection. Adv Compo Hybrid Mater 5:1196–1205. https://doi.org/10.1007/s42114-022-00472-9

28. Liu X, Wu Z, Jiang D, Guo N, Wang Y, Ding T, Weng L (2022) A highly stretchable, sensing durability, transparent, and environmentally stable ion conducting hydrogel strain sensor built by interpenetrating Ca^{2+}-SA and glycerol-PVA double physically cross-linked networks. Adv Compo Hybrid Mater 5:1712–1729. https://doi.org/10.1007/s42114-021-00396-w
29. Cheng K, Zou L, Chang B, Liu X, Shi H, Li T, Yang Q, Guo Z, Liu C, Shen C (2022) Mechanically robust and conductive poly(acrylamide) nanocomposite hydrogel by the synergistic effect of vinyl hybrid silica nanoparticle and polypyrrole for human motion sensing. Adv Compo Hybrid Mater 5:2834–2846. https://doi.org/10.1007/s42114-022-00465-8
30. Bakadia BM, Zhong A, Li X, Boni BOO, Ahmed AAQ, Souho T, Zheng R, Shi Z, Shi D, Lamboni L, Yang G (2022) Biodegradable and injectable poly(vinyl alcohol) microspheres in silk sericin-based hydrogel for the controlled release of antimicrobials: application to deep full-thickness burn wound healing. Adv Compo Hybrid Mater 5:2847–2872. https://doi.org/10.1007/s42114-022-00467-6
31. Zhang F, Lian M, Alhadhrami A, Huang M, Li B, Mersal GAM, Ibrahim MM, Xu M (2022) Laccase immobilized on functionalized cellulose nanofiber/alginate composite hydrogel for efficient bisphenol A degradation from polluted water. Adv Compo Hybrid Mater 5:1852–1864. https://doi.org/10.1007/s42114-022-00476-5
32. Kong D, El-Bahy ZM, Algadi H, Li T, El-Bahy SM, Nassan MA, Li J, Faheim AA, Li A, Xu C, Huang M, Cui D, Wei H (2022) Highly sensitive strain sensors with wide operation range from strong MXene-composited polyvinyl alcohol/sodium carboxymethylcellulose double network hydrogel. Adv Compo Hybrid Mater 5:1976–1987. https://doi.org/10.1007/s42114-022-00531-1
33. Han C, Yang F, Guo X, Bai Y, Liu G, Sun H, Wang P, Liu W, Wang R (2021) Ultra-stretchable self-healing composite hydrogels as touch panel. Adv Mater Interfaces 8:2100742. https://doi.org/10.1002/admi.202100742
34. Roig-Sanchez S, Kam D, Malandain N, Sachyani-Keneth E, Shoseyov O, Magdassi S, Laromaine A, Roig A (2022) One-step double network hydrogels of photocurable monomers and bacterial cellulose fibers. Carbohydr Polym 294:119778. https://doi.org/10.1016/j.carbpol.2022.119778
35. Li T, Wei H, Zhang Y, Wan T, Cui D, Zhao S, Zhang T, Ji Y, Algadi H, Guo Z, Chu L (2023) Sodium alginate reinforced polyacrylamide/xanthan gum double network ionic hydrogels for stress sensing and self-powered wearable device applications. Carbohydr Polym 309:120678. https://doi.org/10.1016/j.carbpol.2023.120678
36. Yan C, Huang J, Cao C, Wang Y, Lin X, Qian X (2022) Response of constructed wetland for wastewater treatment to graphene oxide: perspectives on plant and microbe. J Hazard Mater 422:126911. https://doi.org/10.1016/j.jhazmat.2021.126911
37. Sun J, Zhang X, Du Q, Murugadoss V, Wu D, Guo Z (2021) The contribution of conductive network conversion in thermal conductivity enhancement of polymer composite: a theoretical and experimental study. ES Mater Manuf 13: 53–65. https://doi.org/10.30919/esmm5f450
38. Kachere AR, Kakade PM, Kanwade AR, Dani P, Rondiya SR, Dzade NY, Bhosale SV (2021) Zinc oxide/graphene oxide nanocomposites: synthesis, characterization and their optical properties. ES Mater Manuf 16: 19–29. https://doi.org/10.30919/esmm5f516
39. Liu H, Xu T, Liang Q, Zhao Q, Zhao D, Si C (2022) Compressible cellulose nanofibrils/reduced graphene oxide composite carbon aerogel for solid-state supercapacitor. Adv Compos Hybrid Mater 5:1168–1179. https://doi.org/10.1007/s42114-022-00427-0
40. Gu H, Zhang H, Ma C, Sun H, Liu C, Dai K, Zhang J, Wei R, Ding T, Guo Z (2019) Smart strain sensing organic-inorganic hybrid hydrogels with nano barium ferrite as the cross-linker. J Mater Chem C 7:2353–2360. https://doi.org/10.1039/c8tc05448g
41. Ma J, Xiong Y, Dai X, Yu F (2020) Coadsorption behavior and mechanism of ciprofloxacin and Cu(II) on graphene hydrogel wetted surface. Chem Eng J 380. https://doi.org/10.1016/j.cej.2019.122387
42. Jafari H, Ghaffari-Bohlouli P, Niknezhad SV, Abedi A, Izadifar Z, Mohammadinejad R, Varma RS, Shavandi A (2022) Tannic acid: a versatile polyphenol for design of biomedical hydrogels. J Mater Chem B 10:5873–5912. https://doi.org/10.1039/d2tb01056a
43. Wang Y, Chen S, Zhao S, Chen Q, Zhang J (2020) Interfacial coordination assembly of tannic acid with metal ions on three-dimensional nickel hydroxide nanowalls for efficient water splitting. J Mater Chem A 8:15845–15852. https://doi.org/10.1039/d0ta02229b
44. Tylman M, Pieklarz K, Owczarz P, Maniukiewicz W, Modrzejewska Z (2018) Structure of chitosan thermosensitive gels containing graphene oxide. J Mol Structure 1161:530–535. https://doi.org/10.1016/j.molstruc.2018.02.065
45. Guo X, Ge S, Wang J, Zhang X, Zhang T, Lin J, Zhao CX, Wang B, Zhu G, Guo Z (2018) Waterborne acrylic resin modified with glycidyl methacrylate (GMA): formula optimization and property analysis. Polymer 143:155–163. https://doi.org/10.1016/j.polymer.2018.04.020
46. Jiang H, Yang Y, Lin Z, Zhao B, Wang J, Xie J, Zhang A (2020) Preparation of a novel bio-adsorbent of sodium alginate grafted polyacrylamide/graphene oxide hydrogel for the adsorption of heavy metal ion. Sci Total Environ 744:140653. https://doi.org/10.1016/j.scitotenv.2020.140653
47. Lee S, Lee H, Sim JH, Sohn D (2013) Graphene oxide/poly(acrylic acid) hydrogel by γ-ray pre-irradiation on graphene oxide surface. Macromol Res 22:165–172. https://doi.org/10.1007/s13233-014-2025-x
48. Zhuang Y, Yu F, Ma J (2015) Enhanced adsorption and removal of ciprofloxacin on regenerable long TiO_2 nanotube/graphene oxide hydrogel adsorbents. J Nanomater 2015:1–8. https://doi.org/10.1155/2015/675862
49. Lim M, Choi Y, Kim J, Kim K, Shin H, Kim J, Shin DM, Lee J (2017) Cross-linked graphene oxide membrane having high ion selectivity and antibacterial activity prepared using tannic acid-functionalized graphene oxide and polyethyleneimine. J Membrane Sci 521:1–9. https://doi.org/10.1016/j.memsci.2016.08.067
50. Li F, Wang X, Yuan T, Sun R (2016) A lignosulfonate-modified graphene hydrogel with ultrahigh adsorption capacity for Pb(ii) removal. J Mater Chem A 4:11888–11896. https://doi.org/10.1039/c6ta03779h